

3D Aerosol-Cloud Radiative Interaction Observed in Collocated MODIS and ASTER Images of Cumulus Cloud Fields

GUOYONG WEN, ALEXANDER MARSHAK, ROBERT F. CAHALAN, LORRAINE REMER, AND RICHARD
KLEIDMEN

(For submission to Journal of Geophysical Research)

Popular Summary

Aerosols are tiny particles, other than water or ice, suspended in the atmosphere. Those tiny particles act as “seeds” for water vapor to condense to form clouds. Without aerosols in the atmosphere, it is almost impossible to have clouds. Aerosol amount is an important parameter for cloud study. For the same amount of water vapor, clouds formed in an environment with more aerosols (or “seeds”) would have more droplets with smaller sizes compared to clouds in an environment with less aerosols. Scientists have shown that clouds with more but smaller droplets reflect more sunlight compared to clouds with fewer but larger droplet for the same amount of water. How aerosols can affect the reflectance of clouds is an important topic in climate research.

To study how aerosol can affect the reflectance of cloud on global scale, satellite observation is obviously a good choice since one can have both cloud properties and aerosol amount in the clear region nearby. However, satellites do not directly observe aerosols. Scientist uses reflected sunlight to infer the aerosol amount in the field of view of instrument. In this process, the observed reflected sunlight is compared with pre-calculated (or modeled) values to determine the aerosol amount that produces the best match between the two. This is called aerosol retrieval process.

In the operational aerosol retrieval process, clouds near clear regions are ignored. This may lead to a wrong interpretation of satellite observation. A simple example is the shadowed pixels in a satellite image. Since aerosols reflect sunlight, a larger reflected amount of sunlight observed from the satellite will be interpreted as more aerosols. For the same amount of aerosols, the shadowed pixels look darker than non-shadowed. Since the amount of reflected sunlight is used to infer aerosols, darker pixels would be interpreted as less aerosol amount if nearby clouds are ignored. Similarly, nearby clouds can scatter sunlight into nearby non-shadowed pixels making those pixels look brighter. Hence aerosol in those clear pixels would be mis-interpreted as having more aerosols.

A radiative transfer model that takes into accounts the nearby cloud effects, or 3-dimensional (3D) effects, is used to compute the true reflected sunlight that a satellite should observe. We compared the true reflected sunlight with that computed without nearby clouds for two MODIS and ASTER collocated images in Brazil. We found the difference is significantly large. Based on these findings, we advise scientists to use caution when using the standard method to retrieve aerosols or aerosol products derived from this method.

3D Aerosol-Cloud Radiative Interaction Observed in Collocated MODIS and ASTER Images of Cumulus Cloud Fields

GUOYONG WEN^{1,2}, ALEXANDER MARSHAK¹, ROBERT F. CAHALAN¹,
LORRAINE A. REMER¹, and RICHARD G. KLEIDMAN³

Short title: 3D Cloud and Aerosols

(for submission to Journal of Geophysical Research)

¹ NASA Goddard Space Flight Center, Greenbelt, Maryland.

² Goddard Earth Sciences and Technology Center, U. of Maryland Baltimore County, Maryland.

³ Science Systems and Applications, Inc., Maryland.

Corresponding author address:

Guoyong Wen
NASA/GSFC, Code 613.2
Greenbelt, MD 20771

ABSTRACT

1
2 3D aerosol-cloud interaction is examined by analyzing two images containing
3 cumulus clouds in biomass burning regions in Brazil. The research consists of two parts.
4 The first part focuses on identifying 3D cloud impacts on the reflectance of pixel
5 selected for the MODIS aerosol retrieval based purely on observations. The second part
6 of the research combines the observations with radiative transfer computations to
7 identify key parameters in 3D aerosol-cloud interaction. We found that 3D cloud-
8 induced enhancement depends on optical properties of nearby clouds as well as
9 wavelength. The enhancement is too large to be ignored. Associated biased error in 1D
10 aerosol optical thickness retrieval ranges from 50% to 140% depending on wavelength
11 and optical properties of nearby clouds as well as aerosol optical thickness. We caution
12 the community to be prudent when applying 1D approximations in computing solar
13 radiation in clear regions adjacent to clouds or when using traditional retrieved aerosol
14 optical thickness in aerosol indirect effect research.

15 1. INTRODUCTION

16 Aerosols play a critical role in the process of cloud formation. A change in aerosol
17 properties may lead to a change in microphysical and radiative properties of cloud, and
18 indirectly influence the Earth's climate. Analyzing AEROENET ground-based network
19 Holben [1998], recently Kaufman and Koren [2006] found that absorbing and non-
20 absorbing aerosols affect cloud cover differently. While absorbing aerosols prevent
21 clouds from forming, non-absorbing aerosols extend cloud life times and are associated
22 with enhanced cloud cover. This complements Twomey's [1977] fundamental theory
23 that ties an increase of anthropogenic aerosol to possible consequences to global climate

24 change. An example of an application of this theory is the modification of cloud
25 properties through a change in cloud condensation nuclei (CCN) in ship tracks
26 observed from space [Platnick *et al.*, 2000; Coakley *et al.*, 1987]. However assessing and
27 quantifying the indirect effect of aerosol on cloud properties and climate in global scale
28 still remains a great challenge. The radiative forcing of aerosol indirect effect on climate
29 has been identified as the most uncertain among other radiative forcing factors
30 [Intergovernmental Panel on Climate Change (IPCC), 2001]. For example, the effect of
31 aerosols on cloud albedo has a large range of uncertainties estimated as cooling
32 between -2 and 0 W/m². The level of scientific understanding of aerosol indirect effect
33 is categorized as “very low”. Global observation of aerosol and cloud properties from
34 satellite is one way to advance our understanding of aerosol indirect effect on the
35 Earth’s climate, and to reduce its uncertainties.

36 However, aerosol and cloud property data sets from satellite observation themselves
37 are subject to large uncertainties. This is partly because cloud and aerosol properties
38 are derived from the satellite observed reflected solar radiation using assumptions
39 about the Earth’s surface, atmosphere, aerosols, and clouds. For operational purpose,
40 the atmosphere, aerosols and clouds are usually assumed to be horizontally
41 homogeneous and plane-parallel, which is called the one-dimensional (1D)
42 approximation or plane-parallel approximation (PPA). In this approximation, it is
43 assumed that radiative properties of an individual pixel are independent of its
44 neighbors. Many studies have shown that 3D cloud structure has a complicated impact
45 on retrievals of cloud properties [e.g., Chambers *et al.*, 1997; Varnai and Marshak, 2002;
46 Iwabuchi and Hayasaka, 2002; Horváth and Davies, 2004; Marshak *et al.*, 2006]. In this
47 study, we focus on how 3D cloud structure affect reflectance in the clear region near
48 clouds and what are the consequences of this enhanced reflectance on aerosol retrievals.

49 Aerosol optical thickness (AOT) in the clear region near clouds is a key parameter in
50 the study of aerosol indirect effect from remote sensing instruments. In this region the
51 atmosphere experiences a big change in optical properties with optically thin aerosols
52 surrounded by optically thick clouds. Since clouds, aerosols and molecules all scatter
53 sunlight at wavelengths selected for aerosol retrievals, 3D aerosol-cloud radiative
54 interactions have a large impact on clear region reflectance and thus on associated
55 aerosol retrievals. As we demonstrate in this paper, the conventional 1D retrieval can
56 lead to large biased error in aerosol optical depth. Thus to understand 3D aerosol-cloud
57 radiative interaction, to quantify its impact on aerosol retrievals is important to reduce
58 uncertainties in estimates of aerosol indirect effects on the Earth's climate using satellite
59 observations.

60 3D aerosol-cloud radiative interactions have received increasing attention in the past
61 several years. Efforts were made to parameterize 3D cloud effects on reflectance in
62 clear regions of Landsat ETM+ images [Wen *et al.*, 2001; Nikolaeva *et al.*, 2005]. 3D
63 radiative transfer models were used to compute 3D cloud effects near ideal clouds
64 (infinitely long cuboidal bar cloud, 3D cubic cloud, horizontally semi-infinite cloud)
65 [Kobayashi *et al.*, 2000; Cahalan *et al.*, 2001; Nikolaeva *et al.*, 2005]. Using MODIS 1km
66 resolution cloud optical depth product, and the brightness temperature at 11 microns to
67 construct a realistic 3D cloud field, Wen *et al.* [2006] demonstrated that a 3D cloud has
68 strong impact on the reflected clear sky solar radiation and thus on associated 1D
69 aerosol retrieval.

70 This work is an extension of our previous research. It includes 1) analysis of MODIS
71 aerosol retrievals for possible 3D cloud effects; 2) computation of 3D cloud effects at 0.5
72 km resolution and examination of 3D cloud effects on pixels selected by MODIS aerosol
73 retrieval algorithm; 3) study of 3D cloud effects at a smaller resolution not resolved by

74 MODIS. The study is conducted for two cumulus cloud fields in Brazil. These two
75 cloud fields are distinctive in terms of “large” and “small” aerosol loadings from
76 MODIS retrievals to represent “polluted” and “pristine” scenes respectively.

77 The data sets are described in section 2 followed by data analyses in section 3. Section
78 4 presents 3D cloud radiative effects computed in cloud fields. In the final section the
79 results are summarized and discussed.

80 2. DATA DESCRIPTION

81 Two MODIS nadir viewed scenes from the Terra satellite in biomass burning regions
82 of Brazil were acquired on January 25, 2003 (scene 1) and August 9, 2001 (scene 2). The
83 size of both scenes is 80 km x 68 km. These scenes entirely cover the collocated high-
84 resolution Advanced Spaceborne Thermal Emission and Reflection Radiometer
85 (ASTER) images of size ~60 km x 60 km [Yamaguchi *et al.*, 1998]. Scene 1, used earlier
86 by Wen *et al.* [2006], is centered on the equator at 53.78° west, with solar zenith angle of
87 32° and solar azimuth angle of 129° from north. Scene 2, used earlier by Marshak *et al.*
88 [2006], is centered at 17.1° south and 42.16° west with solar zenith angle of 41°, and solar
89 azimuth angle of 38° from north. The two ASTER images are presented in Fig. 1 and
90 their characteristics described in Table I.

91 The collection 4 of 1-km MODIS retrieved cloud optical depth fields [Platnick *et al.*,
92 2003] of the two scenes are presented in Fig. 2. Cloud fractions in scene 1 and scene 2
93 are 53% and 40%, with average cloud optical depth about 12 and 8, respectively. The
94 MODIS surface albedo [Moody *et al.*, 2005] is used in this study. The surface in scene 1
95 is darker and more homogeneously covered by vegetation as compared to scene 2. The
96 average surface albedo and associated standard deviation for the two visible bands at
97 0.47 μm and 0.66 μm , and the mid-IR band at 2.13 μm are presented in Table II. Scene 1

98 appears to be “polluted” with MODIS retrieved average aerosol optical thickness of 0.37
99 at 0.47 μm and 0.19 at 0.66 μm . Aerosol loading in the “pristine” scene 2 is considerably
100 smaller with average aerosol optical thickness of ~ 0.09 and ~ 0.07 at 0.47 μm and 0.66
101 μm , respectively.

102 Similar to the study conducted by Wen *et al.* [2006], the cloud top height is estimated
103 using the brightness temperature at 11 μm using MODIS band 31; the vertical extinction
104 profile is obtained assuming a linear distribution of cloud liquid water. To be consistent
105 with a resolution of 0.5 km used in the MODIS aerosol retrieval algorithm [Remer *et al.*,
106 2005], a 1 by 1 km resolution pixel is split into four 0.5 by 0.5 km resolution pixels both
107 for atmosphere products and the surface albedo to compute the 3D cloud effects on the
108 reflected solar radiation at 0.47 μm and 0.66 μm of the MODIS band 3 and band 1,
109 respectively.

110 We further examine the 3D cloud effects at a smaller scale not resolved by MODIS.
111 This is motivated by the fact that both cloud optical depth and MODIS retrieved aerosol
112 optical thickness have large spatial variability (Figs. 2 and 3). It appears that cloud
113 optical depth and aerosol amount from MODIS are related. Two regions of scene 1
114 indicated by upper and lower boxes in Fig. 2 are particularly interesting. The lower box
115 has a clear region with relatively large aerosol amount from MODIS (AOT ~ 0.4)
116 surrounded by optically thick clouds with average optical depth of ~ 14 . In the upper
117 box, the clear regions with relatively less aerosol loading from MODIS (AOT ~ 0.3) are
118 next to puffy cumulus with average optical depth of ~ 7 . In this work we retrieve cloud
119 optical depth using 15 m resolution ASTER band 2 (0.66 μm) reflectance, and estimate
120 cloud top height using 90 m resolution ASTER brightness temperature at band 14 (11
121 μm). With the same aerosol properties as those for 0.5 km resolution, we perform

122 radiative computation at 90 m resolution to look into the 3D effects at a scale not
123 resolved by MODIS.

124 3. ANALYSES OF MODIS AEROSOL RETRIEVAL

125 Aerosol optical thickness is operationally retrieved at 0.47 μm and 0.66 μm , MODIS
126 band 3 and band 1, respectively. Details about the MODIS aerosol retrieval algorithm
127 over land can be found in Remer *et al.* [2005]. Here we highlight only several important
128 steps of the retrieval algorithm needed to understand the effect of broken Cu clouds on
129 the retrieval of aerosol optical thickness. After applying the 'cloud mask' procedure
130 [Martins *et al.*, 2002] and rejecting 0.5 by 0.5 km pixels with relatively bright surfaces (at
131 2.1 μm), out of the remaining pixels in each 10 by 10 km area, we further reject 50% of
132 the brightest and 20 % of the darkest pixels. Note that the rejected pixels at 0.47 and
133 0.66 μm wavelength are not necessarily identical. If the number of the 'survived' 0.5 by
134 0.5 km pixels in a 10 by 10 km area is larger than a threshold value (12 pixels in the
135 current algorithm), their reflectance values are averaged and aerosol optical thickness
136 assigned to this 10 by 10 km area is retrieved. In this section we will focus on only
137 those 0.5 by 0.5 km pixels that survived rejection and thus have been selected to
138 contribute to aerosol retrievals.

139 In Fig. 2, the selected for aerosol retrieval pixels are indicated as black. It is evident
140 that the "polluted" scene 1 has much fewer pixels selected for aerosol retrieval
141 compared to the "pristine" scene 2; namely, 82 pixels selected for scene 1 versus 340
142 selected pixels for scene 2. Since the cloud fraction is ~53% for scene 1 and ~40% for
143 scene 2 and each scene contains 160x136 pixels, only ~0.8% and ~2.6% of non-cloudy
144 pixels are selected for aerosol retrieval for the two scenes, respectively.

145 The selected pixels are not uniformly distributed in space. In order to quantify the 3D
146 cloud effects, we need to examine the distributions of the selected pixels, their average
147 reflectance and associated standard deviation, as a function of the distance to the
148 nearest cloud. Figure 4 shows that the distance between the selected clear pixels and
149 the nearest cloudy pixels ranges from 0.5 km to 3.6 km with an average of 2 km and
150 standard deviation of 0.6 km. Cloud were designated by the standard MODIS cloud
151 mask algorithm [Ackerman *et al.*, 1998] and were used to retrieve cloud microphysical
152 properties in Collection 4 [Platnick *et al.*, 2003] (Platnick, personal communication 2006).
153 Note that these are separate cloud identification schemes than the one used internally
154 by the MODIS aerosol algorithm [Remer *et al.*, 2005; Martins *et al.*, 2002]. There is no
155 reason why an aerosol retrieval pixel could not coincide with a pixel identified as cloud
156 by the cloud algorithms. The distribution shows that no aerosol pixels overlap with a
157 cloud pixel and only three pixels are contiguous to clouds. With 6 pixels falling within
158 1 km of a cloud and 3 pixels lying beyond 3 km from cloud edges, about 90% of selected
159 pixels are at a distance between 1 km and 3 km from nearest cloud edges. Note that the
160 distributions of the population of selected clear pixels at the two bands are similar even
161 though the selected clear pixels for the two bands are not necessarily the same.

162 For scene 1 (the "polluted" image), the reflectance from the selected pixels decreases
163 as a function of the distance to the nearest cloud. The rate of decrease of reflectance as
164 determined by the best linear fit is $-0.0009/\text{km}$ for $0.47\ \mu\text{m}$ and $-0.0003/\text{km}$ for $0.66\ \mu\text{m}$.
165 Since the surface is dark and homogeneous, it is very unlikely that the decrease in the
166 reflectance is due to the variability in the surface reflective properties. Also, a detailed
167 examination with high-resolution ASTER image (Sect. 5), shows no evidence for sub-
168 pixel cloud contamination, in which the algorithm's cloud mask fails to identify a

169 clearly identifiable cloud. Therefore, the decrease in reflectance as a function of the
170 distance to the nearest cloud is very likely due to 3D radiative interaction.

171 The surface reflectance of scene 2 (the “pristine” image) is more complicated. The
172 surface is much brighter and more inhomogeneous compared to scene 1. The surface
173 albedo is 0.04, 0.08, and 0.16 with standard deviation of 0.01, 0.02, and 0.04 for 0.47 μm ,
174 0.66 μm , and 2.13 μm bands, respectively. The variability of surface albedo for this
175 scene is so large that a 3D radiative signature of the dependence of the clear sky
176 reflectance on the distance from cloud edges is not detectable. Thus only the
177 distribution of the selected pixels for aerosol retrieval is presented below.

178 Figure 5 shows the distribution of 340 selected clear pixels for aerosol retrieval for
179 scene 2. The average distance between the selected clear sky pixels to the nearest cloud
180 is ~ 2.15 km, which is very close to that in scene 1. The distribution of the nearest cloud
181 distances for scene 2 is broader compared to scene 1 with long tail extended to 6 km.
182 The standard deviation of the distribution is ~ 0.97 km for scene 2 versus ~ 0.6 km for
183 scene 1. In contrast to scene 1, 21 pixels contiguous to clouds as identified by the cloud
184 algorithm were selected for aerosol retrieval. As for scene 1, a detailed examination of
185 the selected clear pixels with the high-resolution ASTER image found no evidence of
186 sub-pixel cloud contamination of those pixels.

187 4. 3D CLOUD EFFECTS AT THE 0.5 KM RESOLUTION

188 An I3RC (Intercomparison of 3D Radiation Codes) [Cahalan *et al.*, 2005] certified
189 Monte Carlo (MC) code for radiative transfer in a 3D cloudy atmosphere [Marshak and
190 Davis, 2005] is used in this study. In contrast to Wen *et al.* [2006] that computed the
191 reflected solar radiation for scene 1 at the 1 km resolution, this section will discuss the
192 radiation fields computed at the instrument resolution of 0.5 km for MODIS aerosol

193 retrieval for both scene 1 and scene 2. We will further examine the details of the 3D
194 cloud effects at 90 m resolution not resolved by MODIS in section 5.

195 Similar to Wen *et al.* [2006], the 1km MODIS cloud optical depth is used with cloud
196 top height estimated from brightness temperature at 11 μm of MODIS band 31 on Terra
197 for both scenes. Other cloud structure assumptions are the following. Cloud base is
198 assumed to be constant at 1 km. Cloud liquid water vertical profile is assumed to be
199 linear. Single scattering properties of clouds such as the phase function and single
200 scattering albedo at two MODIS bands are computed assuming a gamma distribution of
201 cloud droplet with effective radius of 10 μm and effective variance of 0.1 [Hansen,
202 1971].

203 Aerosol particles are assumed to have a lognormal size distribution with standard
204 deviation of 0.6 and modal radius of 0.13 μm , and a single scattering albedo of 0.9. For
205 scene 1, aerosol optical thickness is assumed to be 0.2 at 0.47 μm and 0.1 at 0.66 μm . For
206 scene 2, aerosol optical thickness is assumed to be 0.07 at 0.47 μm and 0.05 at 0.66 μm .
207 For simplicity, the aerosols are assumed to be uniformly distributed in two layers: in a
208 boundary layer below 2 km and in a free troposphere above 2 km. Aerosol optical
209 thickness in the free troposphere is assumed to be 0.01 with all the rest of the aerosols in
210 the boundary layer.

211 Surface albedo fields for from MODIS products [Moody *et al.*, 2005] are used in both
212 scenes. The 1 km resolution MODIS-derived cloud optical properties and surface
213 albedo are split into 0.5 km resolution pixels to compute the reflectance at the two
214 bands for the MODIS aerosol retrievals. With the cloud optical depth field, aerosol and
215 molecular properties, and boundary conditions adequately specified, the MC code
216 computes reflectance r_{3D} over a cumulus cloud field. Without clouds, for the same

217 aerosol and molecular properties, and surface albedo, the MC code also computes
218 reflectance r_{1D} . The 3D cloud effect or the enhancement is defined as reflectance
219 difference between the “true” value r_{3D} and its 1D counterpart r_{1D} .

220 4.1 3D CLOUD EFFECTS FOR SCENE 1

221 Figure 6 illustrates enhancement of reflectance in clear regions due to 3D aerosol-
222 cloud radiative interaction for scene 1. It is evident that clouds enhance reflected solar
223 radiation almost everywhere except shadowed pixels (see also [Nikolaeva *et al.*, 2005]).
224 It is seen that clouds have stronger impact on the average enhancement of reflectance
225 with less variability (the range and standard deviation) at the shorter wavelength
226 compared to the longer wavelength (Fig. 6).

227 Spatial distributions of enhancement for the two wavelengths are similar with
228 strong enhancement in front of the sunlit side of clouds and less enhancement (if any)
229 for shadowed pixels. Away from cloud edges, the enhancement is relatively stronger
230 near optically thick clouds (e.g., the lower box in Fig. 2a) than that near optically thin
231 clouds (e.g., the upper box in Fig. 2a) for both wavelengths. One should note that
232 shadowing reduces reflectance for wavelength at $0.66 \mu\text{m}$ resulting in negative
233 enhancement. At $0.47 \mu\text{m}$ however, even though enhancement is small over the
234 shadowed pixel, the cloud-induced enhancement is positive almost everywhere except
235 for a few isolated shadowed pixels. This is because the surface at $0.47 \mu\text{m}$ is darker than
236 that at $0.66 \mu\text{m}$ with surface albedo of ~ 0.01 versus ~ 0.025 , respectively. For clear
237 atmosphere, a brighter surface has a stronger contribution to the reflectance at the top of
238 the atmosphere than a darker surface. When sunlight is blocked by a cloud, the
239 shadowing effects are expected to be larger over a brighter surface than that over a dark
240 surface. For scene 2 with larger surface albedo at both wavelengths, surface-cloud

241 interaction leads to a reduction of reflectance over shadowed pixels as shown in the
242 next sub-section.

243 The radiative effects of clouds on the reflectance in clear regions can be quantified by
244 the statistics of the enhancement and spatial distribution of non-cloudy pixels in terms
245 of nearest cloud distance similar to Wen *et al.* [2006]. The statistics of the enhancement
246 for all non-cloudy pixels as well as those selected for MODIS aerosol retrieval are
247 presented in Fig. 7 for the two wavelengths. For all non-cloudy pixels, as presented in
248 Figs. 7a, 7c, a common feature of the distribution is the large variability of the
249 enhancement within ~ 1 km from clouds for both wavelengths. In this cloud
250 neighboring area, the large variability is associated with less enhancement or reduction
251 over the shadowed pixels and strong enhancement near the sunlit side of clouds. The
252 average enhancement and associated variability decrease with the nearest cloud
253 distance for both wavelengths around 1 km away from cloud edges. The enhancement
254 reaches an asymptotic value of about 0.01 at $0.47 \mu\text{m}$ and 0.004 at $0.67 \mu\text{m}$ about 3 km
255 away from clouds. It can be shown (e.g., [Wen *et al.*, 1999]) that in 1D retrieval the 3D
256 cloud-induced enhancement of 0.01 and 0.004 in reflectance leads to an overestimation
257 of the aerosol optical thickness of about 0.1 and 0.04 for the two wavelengths,
258 respectively. Compared to the true aerosol optical thickness of 0.2 and 0.1 at the two
259 wavelengths, the aerosol optical thickness retrieval from a 1D model results in 50% and
260 40% biased errors, respectively.

261 It is interesting to examine the statistics of the enhancement for pixels selected by the
262 MODIS aerosol algorithm (Figs. 7b, 7d). It is seen that that the average enhancement for
263 pixels selected by MODIS algorithm is significantly large with similar magnitude of that
264 for all over non-cloudy pixels with a few exceptions. The enhancement of the MODIS
265 pixels resembles closely the enhancement to the pixels in the larger data set, although

266 the enhancement of the MODIS pixels beyond the 2 km mark is slightly higher (~0.001
267 to 0.002) than in the general data set, meaning that the selection process in the MODIS
268 algorithm does not shield the final product from artificial 3D enhancement. The
269 enhancement for MODIS selected pixels has a decreasing trend with the nearest cloud
270 distance for both wavelengths. The trends of the enhancement are very similar to those
271 for reflectance at the two wavelengths in section 3.

272 For all non-cloudy pixels, there is a distinguishable difference in the distributions of
273 the enhancement near cloud edges between the two wavelengths. At 0.66 μm , starting
274 at the nearest cloud distance of 0.5 km, just next to clouds, the average enhancement
275 increases from 0.002 and reaches a maximum of 0.006 at 1 km away from clouds then
276 decreases with the distance from the cloud edges (Fig. 7c). At 0.47 μm , the average
277 enhancement almost monotonically decreases reaching an asymptotic value about 0.01
278 at a distance about 3 km away from clouds (Fig. 7a). Again this difference is primarily
279 due to much stronger reduction over shadowed pixels at 0.66 μm compared to that at
280 0.47 μm . The variability in the enhancement measured by the standard deviation for
281 0.66 μm is about twice as large as that for 0.47 μm in the cloud neighboring area (0.5km
282 – 1km) (Figs. 7a, 7c).

283 The cumulative distribution of all non-cloudy pixels demonstrates that the population
284 of clear pixels decreases rapidly as a function of nearest cloud distance (Fig. 7a). 90% of
285 all clear pixels are within a range of about 1.6 km from cloud edges. Only about 5% of
286 clear pixels are more than 2 km beyond from cloud edges. At a distance of 3 km away
287 from cloud edges there are less than 1% of clear pixels left. Sharp reduction of the
288 number of clear pixels with the distance from cloud edges for Cu clouds were also

289 reported by Joseph and Cahalan [1990] from the Landsat data and by Lane *et al.* [2002]
290 from the ground-based measurements.

291 It is also interesting to note that in this study using 0.5 km resolution data, the cloud
292 neighboring region, a 1 km wide band contiguous to the cloud edges, is narrower than
293 that from 1 km resolution data used in Wen *et al.* [2006]. The apparent wider cloud
294 neighboring area at 1 km resolution image is primarily due to a coarse resolution used
295 in that study. At a resolution coarser than the true shadow size, the entire pixel would
296 be a shadowed pixel even if it were partly shadowed. Thus it is necessary to study 3D
297 aerosol-cloud interaction in a finer scale.

298 **4.1 3D CLOUD EFFECTS FOR SCENE 2**

299 Figure 8 shows images of 3D cloud effects for the “pristine” scene 2. Aerosol optical
300 thickness is assumed to be 0.07 at 0.47 μm and 0.05 at 0.66 μm , slightly less than that
301 from MODIS retrieval at the two wavelengths. Similar to the “polluted” scene 1, clouds
302 enhance the reflected solar radiation almost everywhere except for the shadowed pixels
303 for both wavelengths. From cloud shadows, we can see that the Sun is shining from the
304 northeast when Terra was passing over the scene at about 10:30 am in local time on
305 August 9, 2001 in the southern hemisphere.

306 Clouds in scene 2 have a different pattern compared to scene 1. Clouds are mostly in
307 the right part of the image with small scattered cumuli on the left. The enhancement in
308 clear gaps on the right part of the image is evidently larger than that on the left part.
309 The shadowing reduction and sunlit enhancement can be clearly identified.

310 Similar to scene 1, 3D clouds have stronger impact on the average enhancement of
311 reflectance with less variability (the range and standard deviation) at the shorter
312 wavelength compared to the longer wavelength (Fig. 8). It is interesting to note that at

313 0.66 μm the average enhancement (reduction!) for all non-cloudy pixels is negative (-
314 0.003) with large standard deviation of 0.02. One can see that away from clouds, in the
315 cloud free area on the left side of the image, 3D clouds-induced enhancement appears to
316 be uniform.

317 The enhancement (or reduction) of the reflected radiation from shadowed pixels of
318 scene 2 behaves differently from that in scene 1 at 0.47 μm . In scene 1, the enhancement
319 of shadowed pixels is small but positive almost everywhere. In scene 2, the 3D cloud
320 effects reduce the reflectance over shadowed pixels, resulting in a negative
321 enhancement or reduction. The shadowing reduction of reflectance is primarily
322 associated with a brighter surface in scene 2. With average surface albedo ~ 0.01 in
323 scene 1 versus ~ 0.04 in scene 2, the surface in scene 1 is much darker than that in scene 2
324 at 0.47 μm .

325 The distributions of the enhancement of reflectance for the two wavelengths and
326 populations of all non-cloudy pixels and those selected by MODIS aerosol retrieval
327 algorithm are presented as a function of the nearest cloud distance (Fig. 9). For all non-
328 cloudy pixels (Figs 9a, 9c), the enhancement at the two wavelengths shows similar
329 distribution as a function of nearest cloud distance. Large variability associated with
330 reduction over shadowed pixels and strong enhancement in front of sunlit side of
331 clouds is seen within ~ 1.5 km of cloud edges. A wider cloud neighboring area
332 compared to scene 1 is primarily due to a larger solar zenith angle of $\sim 40^\circ$ in scene 2
333 compared to a smaller solar zenith angle of $\sim 30^\circ$ in scene 1. Similar to scene 1, the
334 variability of the enhancement for 0.66 μm in the cloud neighboring area (0.5-1.5km) is
335 twice as large as that for 0.47 μm (Figs. 9a, 9c). The variability drops quickly in the first
336 couple of kilometers from clouds. The average enhancement increases reaching a

337 maximum at a distance 1.5 km away from cloud edges, then decreases gradually to
338 asymptotic value of ~ 0.006 at $0.47 \mu\text{m}$ and ~ 0.003 at $0.66 \mu\text{m}$ at a distance about 3 km
339 away from cloud edges. The enhancement of 0.006 and 0.003 can be translated to
340 overestimate of aerosol optical thickness of 0.06 and 0.03 if 3D aerosol-cloud radiative
341 interaction is ignored. Compared to the true aerosol optical thickness of 0.07 at $0.47 \mu\text{m}$
342 and 0.05 at $0.66 \mu\text{m}$, 1D approximation overestimates aerosol optical thickness by 86%
343 and 60% at the two wavelengths, respectively.

344 The distributions of the enhancement for pixels selected by MODIS aerosol retrieval
345 algorithm are illustrated in Figs. 9b, 9d. With more samples for the selected pixels, the
346 distributions of the average enhancement and variability for the subset resemble those
347 of the larger population of all non-cloudy pixels (Figs. 9a, 9c). However, there is a
348 distinctive difference between the distributions for MODIS selected pixels and their
349 counterparts for overall non-cloudy pixels. The distribution of the enhancement for the
350 selected pixels reaches asymptotic value at a distance about 2 km away from cloud
351 edges, rather than 3 km for overall non-cloudy pixels. For the selected pixels, the
352 asymptotic enhancement is 0.0075 and 0.0041 for wavelength at $0.47 \mu\text{m}$ and $0.66 \mu\text{m}$
353 respectively. Compared with the asymptotic enhancements of 0.006 and 0.0029 for the
354 same wavelength, we found that the average enhancement for MODIS selected pixels is
355 about 0.0015 and 0.0012 larger than that for the overall non-cloudy pixels. Again, the
356 pixel selection process in the MODIS aerosol algorithm does not eliminate significant
357 enhancement of reflectance by 3D effects.

358 The overall population of clear pixels decreases away from cloud edges at a slower
359 rate compared to scene 1. At a distance 3 km away from cloud edges, where the
360 enhancement reaches asymptotic values, there are still about 10% of clear pixels left. At

361 a distance 3.5 km, the clear pixel population drops to 5%. At a distance beyond 4.6 km
362 from cloud edges, only 1% of clear pixels are left. It is also interesting to note that even
363 at a distance about 6-8 km away from clouds, the enhancement does not vanish. Thus
364 under any circumstances, asymptotic enhancement of reflectance in clear regions of a
365 cloudy atmosphere is very large, producing a biased aerosol retrieval from the 1D
366 approximation.

367 5. 3D CLOUD EFFECTS AT 90M RESOLUTIONS

368 As demonstrated above, spatial resolution is important when the scale of true
369 variation is unresolved by instrument resolution. Examples of MODIS unresolved
370 features are the size of cloud shadows, and clouds smaller than 0.5 km in size. Cloud
371 optical depth and cloud structure also vary in space. Distributions of the enhancement
372 for scene 1 and scene 2 in section 4 describe the statistics for the whole image at 0.5 km
373 MODIS resolution. To better understand the cloud effects on reflectance in nearby clear
374 regions, we have to study 3D radiative transfer at small scales unresolved by MODIS.

375 In this study, the radiance at 0.66 μm from a simultaneous ASTER image is used to
376 retrieve cloud optical thickness. The original 15 m resolution ASTER image is
377 aggregated to the 90 m resolution image. Cloud optical depth fields retrieved from
378 ASTER for the two sub-images of MODIS highlighted in Fig. 2a are presented in Fig. 10.
379 There are three features to mention. First, clouds in the lower sub-image are optically
380 thick compared to those in the upper sub-image. The average cloud optical depth ($\tau \sim 14$)
381 in the thick cloud field is twice as large as that ($\tau \sim 7$) in the thin cloud field. Second, the
382 difference in cloud coverage is not dramatic between the two fields with $\sim 59\%$ and
383 $\sim 51\%$ for the thick clouds and the thin clouds respectively. Third is that the small puffy

384 cumuli not identified in the MODIS cloud optical depth product are now resolved by
385 ASTER.

386 The same amount of aerosols for the scene 1 study and the same average surface
387 albedo are used in computing 3D radiation fields for both sub-images for the pair of
388 wavelengths. The results are presented in Fig. 11 for thin (upper panel) and thick
389 (lower panel) cloud fields for the two wavelengths. Similar to the coarse resolution
390 image, except for shadowed pixels at 0.66 μm , clouds enhance the reflectance almost
391 everywhere in clear regions for both wavelengths. Small positive enhancement of
392 reflectance over shadowed pixels at 0.47 μm is primarily due to very low surface albedo
393 as explained earlier.

394 Near cloud edges, the enhancement of shadowed and sunlit sides is not uniformly
395 distributed. It is clear from those images that the impact due to 3D clouds does indeed
396 depend on the resolution. Small clouds and their shadows are evidently unresolvable
397 by MODIS with 0.5 km resolution. Large variability of the enhancement near cloud
398 edges in the MODIS resolution of 0.5 km (see Figs. 6, 7) can be explained by the non-
399 uniform variability at a smaller scale.

400 The enhancement clearly depends on the optical depth of the nearby cloud field as
401 well as wavelength. Similar to the coarse resolution, clouds have stronger impact with
402 less variability (the range and standard deviation) on the average enhancement of
403 reflectance at the shorter wavelength compared to the longer wavelength for the same
404 cloud field (Fig. 11). It is interesting to note that at 0.66 μm the average enhancement is
405 small (0.0018) with large standard deviation of 0.007 in the thin cloud field. It is seen
406 that the average enhancement increases by 50% and 5 times from thin clouds to thick
407 clouds for wavelengths 0.47 μm and 0.66 μm respectively.

408 Distributions of enhancement and associated clear populations are presented in Fig.
409 12. It is evident that enhancement has large variability within the first 1 km from cloud
410 edges, and reaches asymptotic values beyond 1km. For the same reason as in the coarse
411 resolution, the large variability near cloud edges is primarily due to the strong diffuse
412 enhancing in front of sunlit side of clouds and less enhancement or even reduction of
413 shadowing effects. The relatively brighter surface at 0.66 μm compared to that at 0.47
414 μm is the cause of larger variability even negative enhancement at the longer
415 wavelength. (See the standard deviations in the cloud neighboring region in Fig. 12).

416 Away from the extremes of 3D impacts in the cloud neighboring region, the
417 asymptotic values can be used to estimate 3D cloud-induced enhancement. Again, the
418 asymptotic values depend on wavelength as well as optical depth of nearby cloud
419 fields. For the thin clouds, the asymptotic values of the enhancement are 0.012 and
420 0.0046 for wavelengths 0.47 μm and 0.66 μm , respectively (Fig. 12a, 12b). For the thick
421 cloud field, the asymptotic values of the enhancement are 0.019 and 0.014 for 0.47 μm
422 and 0.66 μm respectively (Fig. 12c, 12d). Since the true aerosol optical thickness is 0.2
423 and 0.1 for the two wavelengths, the 1D approximation will overestimate aerosol optical
424 thickness by ~ 0.12 for 0.47 μm and ~ 0.05 for 0.66 μm in the thin cloud field, about 50%
425 larger than the true values. In the thick cloud field, ignoring 3D aerosol-cloud radiative
426 effects will lead to overestimates of aerosol optical thickness of about ~ 0.2 for 0.47 μm
427 and ~ 0.14 for 0.66 μm . The systematic bias errors for thick clouds are $\sim 100\%$ and $\sim 140\%$
428 for the two wavelengths, respectively.

429 6. SUMMARY AND DISCUSSIONS

430 Two MODIS and ASTER collocated images of cumulus clouds are analyzed to study
431 3D cloud-aerosol radiative interaction and its impact on aerosol retrievals. Our studies

432 show that 3D clouds enhance reflectance almost everywhere in clear pixels in cumulus
433 fields except for shadowed pixels. The major factors that determine the magnitude of
434 the enhancement are (1) the distance between the clear pixel and surrounding clouds –
435 farther away from clouds the less the variability and the enhancement; (2) optical
436 properties of surrounding clouds – the thicker the clouds, the larger the enhancement;
437 (3) the wavelength considered – the shorter the wavelength, the larger the
438 enhancement; (4) surface albedo – the larger the surface albedo, the larger the
439 enhancement.

440 By visually examining pixels selected for MODIS aerosol retrievals with collocated
441 high-resolution ASTER images, we did not find evidence of cloud contamination for
442 those selected pixels. This means none of those pixels selected for the aerosol retrieval
443 coincided with a cloud as identified with the high resolution ASTER. We found that
444 both the observed reflectance and 3D clouds-induced enhancement have a slightly
445 decreasing wavelength dependent trend with the distance from the nearest cloud edge
446 in scene 1. Since the surface is dark and homogeneous at the two wavelengths and there
447 is no cloud contamination for those selected pixels, wavelength dependent decreasing
448 trends are likely due to 3D cloud effects.

449 Away from cloud edges where extreme situations of the 3D radiative effects occur, the
450 asymptotic enhancement provides an estimate of 3D effects on both the radiation field
451 and on aerosol retrievals from that field. For aerosol optical thickness of 0.2 at $0.47\ \mu\text{m}$
452 in the “polluted” scene at 0.5 km resolution, we found that the overestimation of aerosol
453 optical thickness will be about +0.1 (absolute) or +50% (relative) using a 1D retrieval,
454 which is about the same as that in the thin cloud field in the 90 m study. This biased
455 error almost doubles in the thick cloud field. At the longer wavelength of $0.66\ \mu\text{m}$, the

456 1D approximation leads to a less but still appreciably large systematic biased error
457 (+40% in thin cloud field and +140% in thick cloud field) in aerosol optical thickness
458 retrieval.

459 3D cloud-induced enhancement in the “pristine” scene is smaller compared to that in
460 the “polluted” scene. But the asymptotic enhancement does not vanish even at a
461 distance 6~8 km away from clouds. The biased error is about +85% and +60% of the
462 ambient aerosol amount for wavelength 0.47 μm and 0.66 μm respectively. We
463 examined the enhancement for MODIS selected pixels for the two scenes. We found
464 that the enhancement of MODIS selected pixels has similar magnitude to or even
465 slightly larger ($\sim 0.001\text{-}0.002$) than the enhancement determined from all non-cloudy
466 pixels for both scenes.

467 One should note that the biased errors for “pristine” scene or “polluted” scene at 0.66
468 μm are close to the upper bound of expected uncertainty of MODIS aerosol retrieval of
469 $\pm 0.05 \pm 0.15\tau$ [Remer *et al*, 2005]. In those cases, although the absolute value of the error is
470 small ($\Delta\tau \sim +0.05$), it is significantly large because the error is biased. This also indicates
471 that the radiative effect of 3D clouds is a potential source of error in long term MODIS
472 aerosol statistics. Combining the analyses of scene 1, scene 2, and thin and thick cloud
473 fields, we conclude that the 3D cloud-induced biased error from 1D retrieval ranges
474 from 50% to 140%.

475 The results in this study are based on two images. In the real atmosphere, cloud
476 properties change from scene to scene. However, the two scenes analyzed here span a
477 broad range of cloud optical properties found in typical broken cumulus fields. Scene 1
478 represents a situation of clear regions completely surrounded by cumulus. In scene 2,
479 most clear pixels are on one half of the image with most cloudy pixels on the other half.

480 Particularly, the detailed studies at 90 m provide the range of the 3D cloud-induced
481 enhancement for thin and thick clouds. The surface albedo differs from scene 1 to scene
482 2. The surface of scene 1 is dark and homogeneous. The surface of scene 2 is brighter
483 and more variable compared to scene 1. Aerosol loadings and surface properties are
484 also different for the two images. We expect that the range of enhancement of aerosol
485 optical thickness retrievals (50% to 140%) found in this study to apply in most situations
486 of broken cumulus.

487 Finally, we conclude that 3D aerosol-cloud radiative interaction enhances extensively
488 the reflectance in clear regions around broken clouds. The 3D cloud-induced
489 enhancement depends on optical properties of nearby clouds as well as wavelength.
490 Radiative effects of 3D clouds are important in understanding of aerosol indirect effects
491 on climate from satellite observations. Thus one should be cautious in applying the 1D
492 approximation to compute clear sky solar radiation in cumulus fields or using aerosol
493 products derived from the 1D approximation in aerosol indirect effect research.

494 *Acknowledgments.* This research was supported by funding provided by NASA and
495 DoE's ARM program.

496 **REFERENCES**

- 497 Ackerman, S. A., K. I. Strabala, W. P. Menzel, R. A. Frey, C. C. Moeller, and L. E.
498 Gumley, Discriminating clear sky from clouds with MODIS. *J. Geophys. Res.*, 103,
499 32141-32157, 1998.
- 500 Andreae, M. O., D. Rosenfeld, P. Artaxo, A.A. Costa, G.P. Frank, K.M Longo, M.A.F.
501 Silva-Dias, Smoking Rain Clouds over the Amazon, *Science* 27 February 2004; 303:
502 1337-1342, DOI: 10.1126/science.1092779.

503 Cahalan, R. F., L. Oreopoulos, A. Marshak, K. F. Evans, A. Davis, R. Pincus, K. Yetzer, B.
504 Mayer, R. Davies, T. Ackerman, H. Barker, E. Clothiaux, R. Ellingson, M. Garay, E.
505 Kassianov, S. Kinne, A. Macke, W. O'Hirok, P. Partain, S. Prigarin, A. Rublev, G.
506 Stephens, F. Szczap, E. Takara, T. Varnai, G. Wen, and T. Zhuravleva, 2005: The
507 International Intercomparison of 3D Radiation Codes (I3RC): Bringing together the
508 most advanced radiative transfer tools for cloudy atmospheres. *Bull. Amer. Meteor.*
509 *Soc.*, **86** (9), 1275-1293

510 Chambers, L. H., B. A. Wielicki, and K. F. Evans, Accuracy of the independent pixel
511 approximation for satellite estimates of oceanic boundary layer cloud optical depth, *J.*
512 *Geophys. Res.*, 102, pp. 1779-1794, 1997.

513 Coakley, J. A., Jr., R. L. Bernstein, and P. A. Durkee, Effect of ship-track effluents on
514 cloud reflectivity, *Science*, 237, 1020-1022, 1987.

515 Feingold, G., Modeling of the first indirect effects: Analysis of measurement
516 requirements, *Geophys. Res. Lett.*, 30(19), 1997, doi:10.1029/2003GL017967, 2003.

517 Han, Q., W. Rossow, and A. Lacis, Near-global survey of effective droplet radii in liquid
518 water cloud using ISCCP data, *Journal of Climate*, 7, 465-497, 1994.

519 Hansen, J., Multiple scattering of polarized light in planetary atmospheres. Part II.
520 Sunlight reflected by terrestrial water clouds, *J. Atmos. Sci.*, **28**, 1400-1426, 1971.

521 Horváth, A., and R. Davies, Anisotropy of water cloud reflectance: A comparison of
522 measurements and 1D theory, *Geophys. Res. Lett.*, 31, L01102,
523 doi:10.1029/2003GL018386, 2004.

524 Iwabuchi, H., and T. Hayasaka, A multi-spectral non-local method for retrieval of
525 boundary layer cloud properties from optical remote sensing data, *Remote Sens.*
526 *Environ.*, **88**, 294 – 308, 2003.

527 Intergovernmental Panel on Climate Change (IPCC), Climate Change 2001: The

528 Scientific Basis. Contribution of Working Group I to the Third Assessment Report of
529 the Intergovernmental Panel on Climate Change, J. T. Houghton, Y. Ding, D. J.
530 Griggs, M. Noguer, P. J. van der Linden, X. Dai, K. Maskell, and C. A. Johnson, eds.,
531 881 pp., Cambridge University Press, New York, 2001.

532 Joseph, J.H. and R.F. Cahalan, Nearest Neighbor Spacing of Fair Weather Cumulus
533 Clouds, *J. Appl., Meteor.*, 29, 793-805, 1990.

534 Kaufman, Y., and R. Fraser, The effect of smoke particles on clouds and climate forcing,
535 *Science*, 277, 1636-1639, 1997.

536 Kaufman, Y., and 11 other coauthors, A critical examination of the residual cloud
537 contamination and diurnal sampling effects on MODIS estimates of aerosol over
538 ocean, *IEEE Trans. Geosci. Remote Sensing*, accepted, 2005.

539 Kobayashi, T., K. Masuda, M. Sasaki, J. Mueller, Monte Carlo simulations of enhanced
540 visible radiance in clear-air satellite fields of view near clouds, *Journal of Geophysical*
541 *Research*, Volume 105, Issue D21, p. 26569-26576, 2000.

542 Lane D.E., K. Goris, and R.C.J. Somerville, Radiative Transfer through Broken Clouds:
543 Observations and Model Validation, *J. Climate.*, 15, 2921-2933, 2002.

544 Marshak, A. and A. Davis, *3D Radiative Transfer in Cloudy Atmospheres*, Springer. 2005.

545 Marshak, A., S. Platnick, T. Varnai, G. Wen, and R. F. Cahalan, Impact of 3D radiative
546 effects on satellite retrievals of cloud droplet sizes, *J. Geophys. Res.*, **111**, DO9207,
547 doi:10.1029/2005JD006686, 2006.

548 Moody, E. G., M. D. King, S. Platnick, C. B. Schaaf, and F. Gao, Spatially complete
549 global spectral surface albedos: Value-Added datasets derived from Terra MODIS
550 land products. *IEEE Trans. Geosci. Remote Sens.*, **43**, 144-158, 2005.

551 Nikolaeva O. V., L.P. Bass, T.A. Germogenova, A.A. Kokhanovisky, V.S. Kuznetsov, B.
552 Mayer, The influence of neighboring clouds on the clear sky reflectance with the 3-D
553 transport code RADUGA. *J. Quant. Spectros. Radiat. Transfer.*, **94**, 405-424, 2005.

554 Platnick, S., P. A. Durkee, K. Nielson, J. P. Taylor, S. C. Tsay, M. D. King, R. J. Ferek, P.
555 V. Hobbs, and J. W. Rottman, The role of background cloud microphysics in the
556 radiative formation of ship tracks, *J. Atmos. Sci.*, **57**, 2607-2624, 2000.

557 Platnick, S., M. King, S. Ackerman, W. P. Menzel, B. Baum, J. C. Riedi, and R. A. Frey,
558 The MODIS cloud products: algorithms and examples from Terra, *IEEE Trans. Geosci.*
559 *Remote Sensing*, vol 41, 459-473, 2003.

560 Remer, L., and 12 other coauthors, The MODIS Aerosol Algorithm, Products, and
561 Validation, *J. Atmos. Sci. Special Section*, vol 62, 947-973, 2005.

562 Twomey, S., The influence of pollution on the shortwave albedo of clouds, *J. Atmos. Sci.*,
563 vol 34, 1149-1152, 1977.

564 Varnai, T., and A. Marshak, Observations of three-dimensional radiative effects that
565 influence MODIS cloud optical thickness retrievals. *J. Atmos. Sci.*, **59**, 1607-1611, 2002.

566 Yamaguchi, Y., A. B. Kahle, H. Tsu, T. Kawakami, and M. Pniel, Overview of Advanced
567 Spaceborne Thermal Emission and Reflection Radiometer (ASTER), *IEEE Trans.*
568 *Geosci. Remote Sensing*, vol 36, 1062-1071, 1998.

569 Wen, G., S-C Tsay, R. F. Cahalan, and L. Oreopoulos, Path radiance technique for
570 retrieving aerosol optical thickness over land, *J. Geophys. Res.*, **104**, 31,321-31,332, 1999.

571 Wen, G., R. F. Cahalan, S-C Tsay, and L. Oreopoulos, Impact of cumulus cloud
572 spacing on Landsat atmospheric correction and aerosol retrieval, *J. Geophys. Res.*, **106**,
573 12,129-12,138, 2001.

574 Wen, G., A. Marshak, and R. F. Cahalan, Impact of 3D Clouds on Clear Sky Reflectance
575 and Aerosol Retrieval in a Biomass Burning Region of Brazil, *IEEE Geo. Rem. Sens.*
576 *Lett.*, **3**, 169-172. 2006.

Table I. Information about the two scenes with solar zenith angle (SZA), solar azimuth angle (SAZ), cloud cover, cloud optical depth (COD) with the average followed by the standard deviation.

	Date Acquired	Center (lat,lon)	SZA	SAZ	Cloud cover	COD
Scene 1	January 25, 2003	(0.N, 53.78W)	32°	129°	53%	$\tau=12, \sigma=10$
Scene 2	August 9, 2001	(17.1S, 42.16 W)	41°	38°	40%	$\tau=8, \sigma=8$

Table II. Average and associated standard deviation of surface albedo of visible and mid-IR bands for scene 1 and scene 2, estimated from Moody *et al.* [2005].

	0.47 μm	0.65 μm	2.13 μm
Scene 1	$\alpha=0.011, \sigma=0.003$	$\alpha=0.025, \sigma=0.004$	$\alpha=0.055, \sigma=0.006$
Scene2	$\alpha=0.039, \sigma=0.009$	$\alpha=0.079, \sigma=0.018$	$\alpha=0.163, \sigma=0.035$

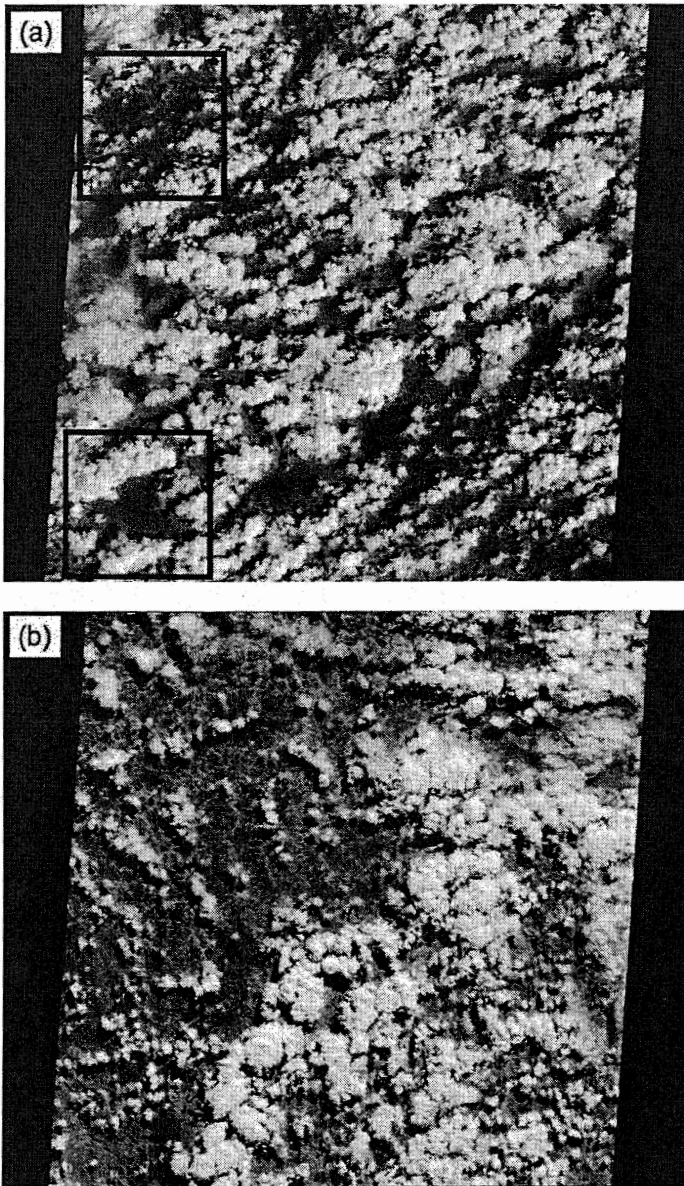


Figure 1. (a) ASTER image of scene 1 centered at $(0^{\circ}\text{N}, 53.78^{\circ}\text{W})$ acquired on January 25, 2003; (b) of scene 2 centered at $(17.1^{\circ}\text{S}, 42.16^{\circ}\text{W})$ acquired on August 9, 2001. Two black boxes in (a) show the regions for detail analysis. The solar zenith angle is 32° and 41° for image (a) and (b) respectively. $\text{RGB}=(2.1\mu\text{m},0.86\mu\text{m},0.55\mu\text{m})$ for both images.

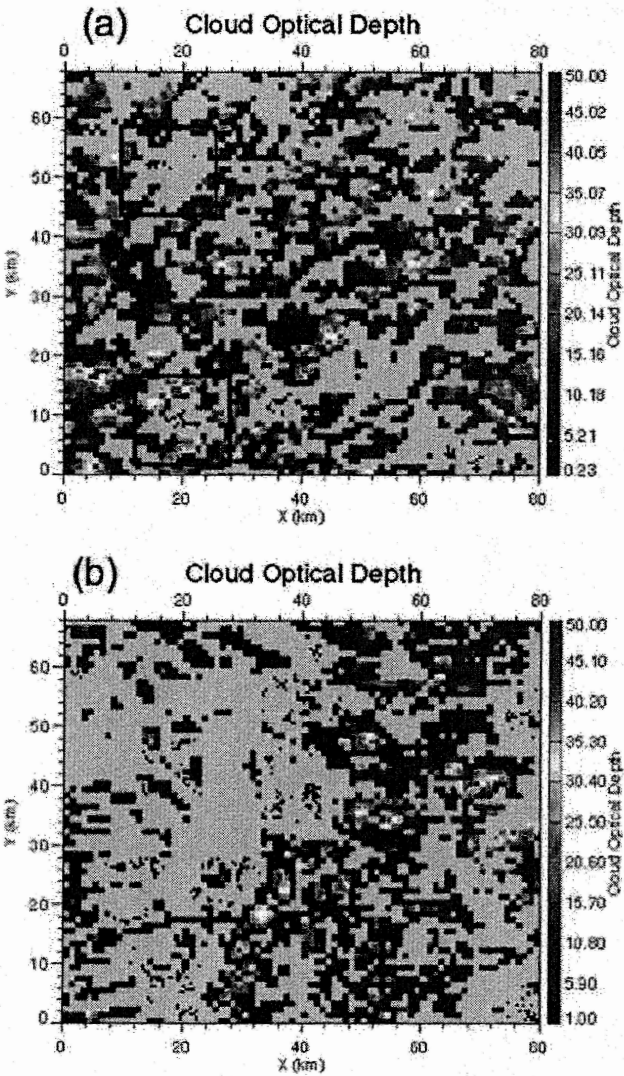


Figure 2. MODIS cloud optical depth fields for collocated ASTER images in Fig. 1 with (a) for scene 1; and (b) for scene 2. The average cloud optical depth and standard deviation are $\tau(\text{scene 1}) \sim 12$ and $\sigma(\text{scene 1}) \sim 10$; $\tau(\text{scene 2}) \sim 8$ and $\sigma(\text{scene 2}) \sim 8$. The cloud cover is $\sim 53\%$ and $\sim 40\%$ for image (a) and (b) respectively. Two squares outlined in black in (a) show the regions for detail analysis. The small black points indicate the 500 m pixels from which the MODIS aerosol products were retrieved.

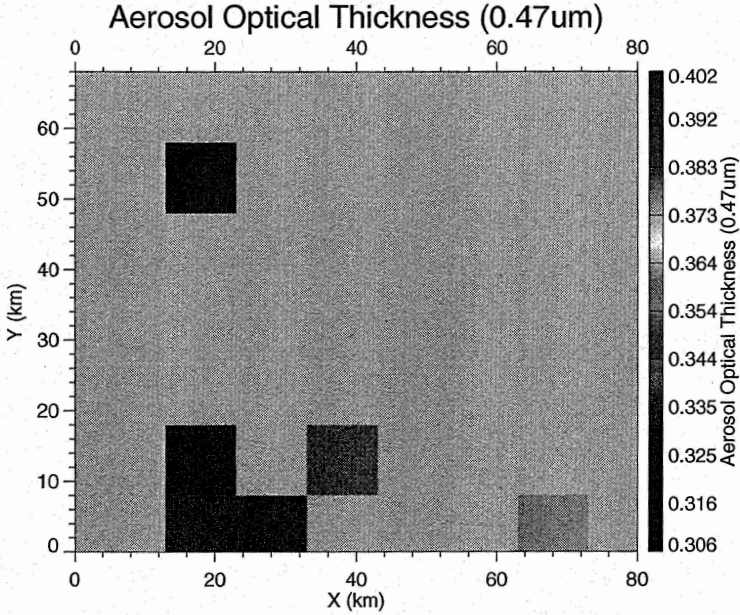


Figure 3. MODIS retrieved aerosol optical thickness for scene 1 in Fig. 2 (a). Aerosol optical thickness of ~ 0.4 near thick clouds (lower box in Fig. 2(a)) is evidently larger than optical thickness (~ 0.3) near thin clouds (upper box of Fig. 2(a)).

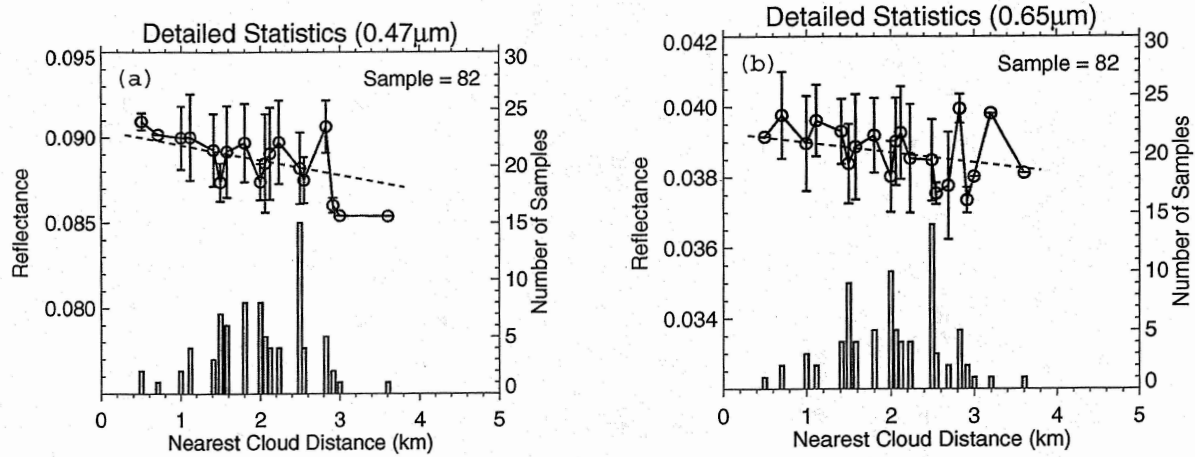


Figure 4. Averaged reflectance (circle, left scale) and standard deviation (vertical brackets, left scale) for pixels for aerosol retrieval for wavelength $0.47 \mu\text{m}$ (a), and $0.66 \mu\text{m}$ (b) of scene 1. Vertical bars show the distribution of those selected pixels (right scale) as a function of the nearest cloud distance. The average of the nearest cloud distance is $\sim 2\text{km}$ with standard deviation of $\sim 0.6\text{km}$. The slope of the best linear fit is about $-0.0009/\text{km}$ at $0.47 \mu\text{m}$ and $-0.0003/\text{km}$ at $0.66 \mu\text{m}$. The average surface albedo and standard deviation are $\alpha_{0.47\mu\text{m}} = 0.011$, $\sigma_{0.47\mu\text{m}} = 0.003$; $\alpha_{0.66\mu\text{m}} = 0.025$, $\sigma_{0.66\mu\text{m}} = 0.004$.

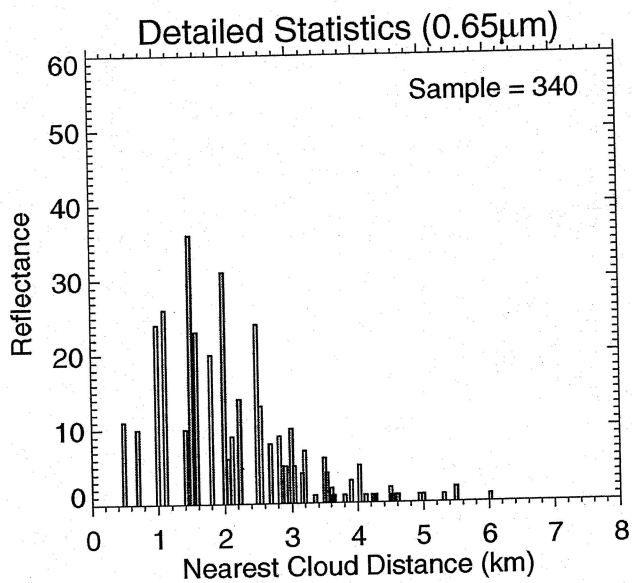


Figure 5. Distribution of selected pixels as a function of the nearest cloud distance at 0.66 μ m wavelength for scene 2. The average of the nearest cloud distance is ~ 2.15 km with standard deviation of ~ 0.97 km. The average surface albedo and standard deviation are $\alpha_{0.47\mu\text{m}} = 0.039$, $\sigma_{0.47\mu\text{m}} = 0.009$; $\alpha_{0.66\mu\text{m}} = 0.079$, $\sigma_{0.66\mu\text{m}} = 0.018$.

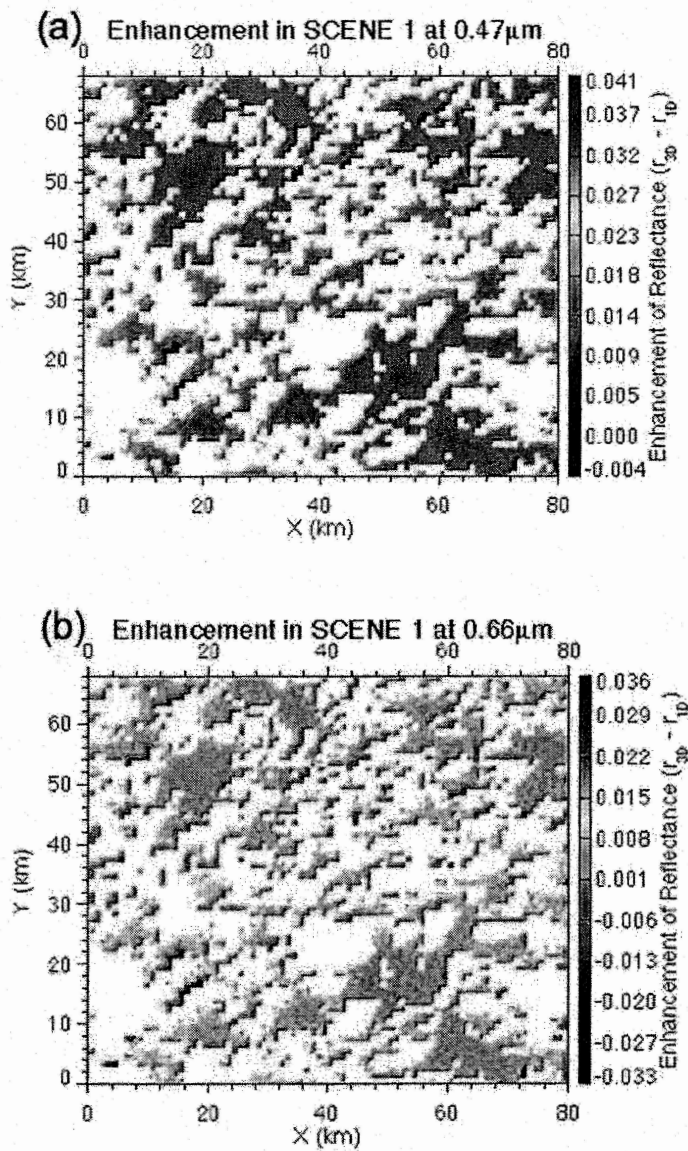


Figure 6. (a) Enhancement of reflected solar radiation due to 3D effects for clear regions in the cumulus field for 0.47 μm , and (b) for 0.66 μm . The direction of incident solar radiation is towards the southeast with a solar azimuth angle of 129° defined from the north. Cloud pixels are masked as white. The averages and associated standard deviations of the enhancement are $\overline{\Delta r}_{0.47\mu\text{m}} = 0.015$ and $\sigma_{0.47\mu\text{m}} = 0.005$; and $\overline{\Delta r}_{0.66\mu\text{m}} = 0.004$ and $\sigma_{0.66\mu\text{m}} = 0.008$. The color bar on (a) and (b) are different.

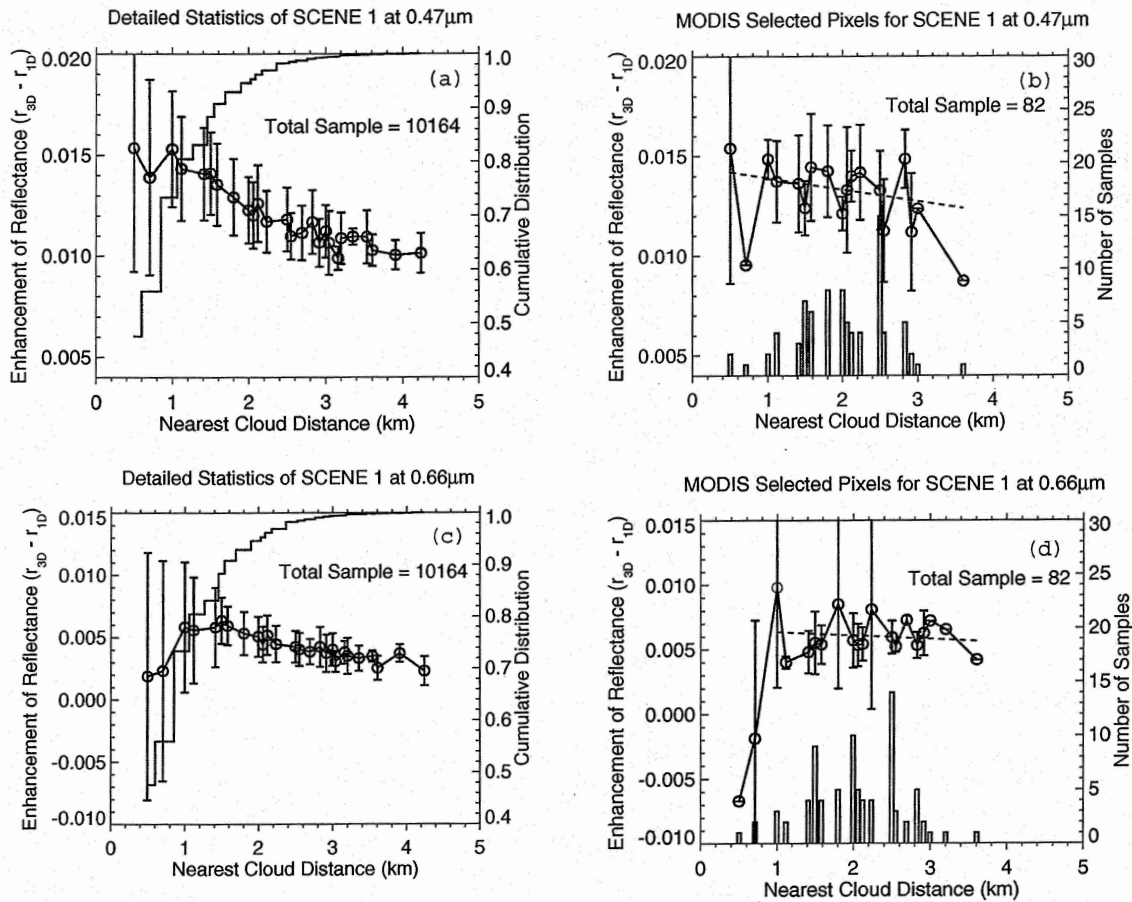


Figure 7. Average enhancement (circles, left scale) and standard deviation (vertical brackets) for clear pixels as a function of the nearest cloud distance. Cumulative and sample distributions of clear pixels as a function of the nearest cloud distance (right scale) for scene 1. Results are (a) and (c) for all non-cloudy pixels at wavelengths 0.47 μ m and 0.66 μ m respectively. Results for MODIS selected pixels are presented in (b) and (d) respectively. The slope of the best linear fit for the MODIS pixels is about -0.0006/km and -0.0003/km for wavelengths 0.47 μ m and 0.66 μ m respectively. Outliers with nearest cloud distance of 0.5 km and 0.7 km are excluded in computing the slope for 0.66 μ m.

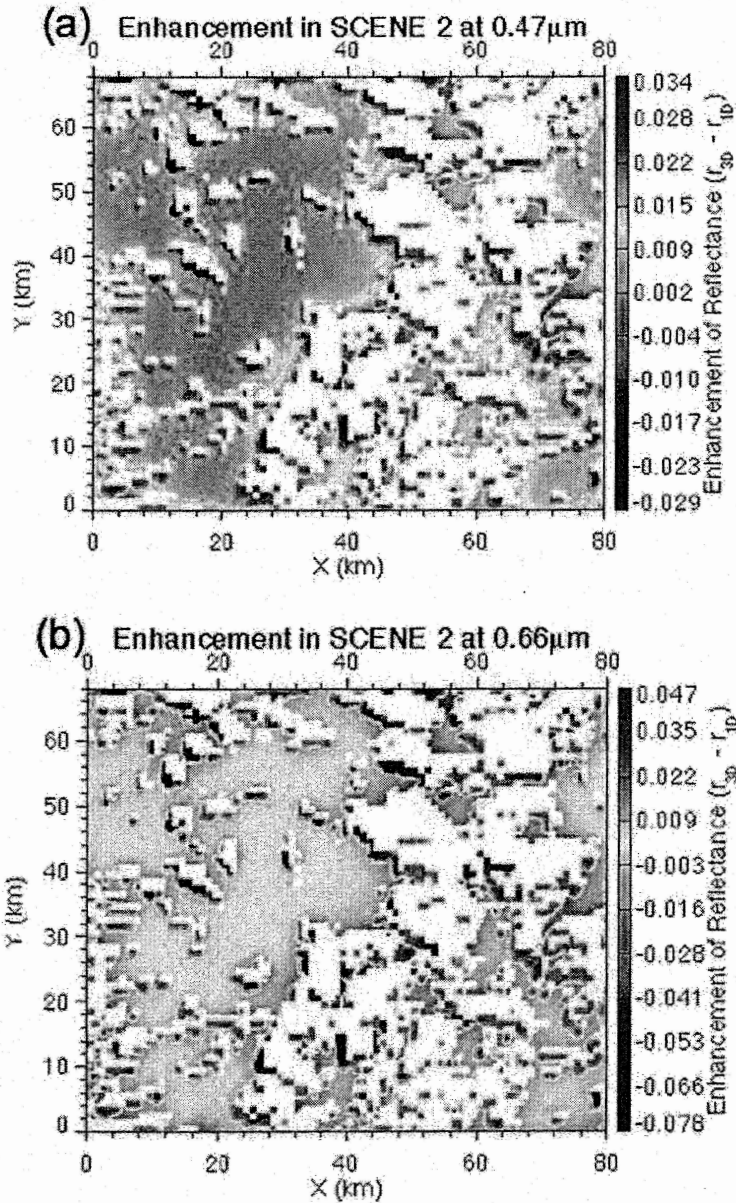


Figure 8. Enhancement of reflected solar radiation due to 3D effects for clear regions in a cumulus field for Scene 2 (a) for $0.47\mu\text{m}$, and (b) for $0.66\mu\text{m}$. The direction of incident solar radiation is from the northeast with solar azimuth angle of 38° from north. Pixels identified as clouds from the MODIS cloud algorithms are masked as white. The averages and associated standard deviations of the enhancement are $\overline{\Delta r_{0.47\mu\text{m}}} = 0.006$ and $\sigma_{0.47\mu\text{m}} = 0.008$; and $\overline{\Delta r_{0.66\mu\text{m}}} = -0.003$ and $\sigma_{0.66\mu\text{m}} = 0.02$, for (a) and (b), respectively.

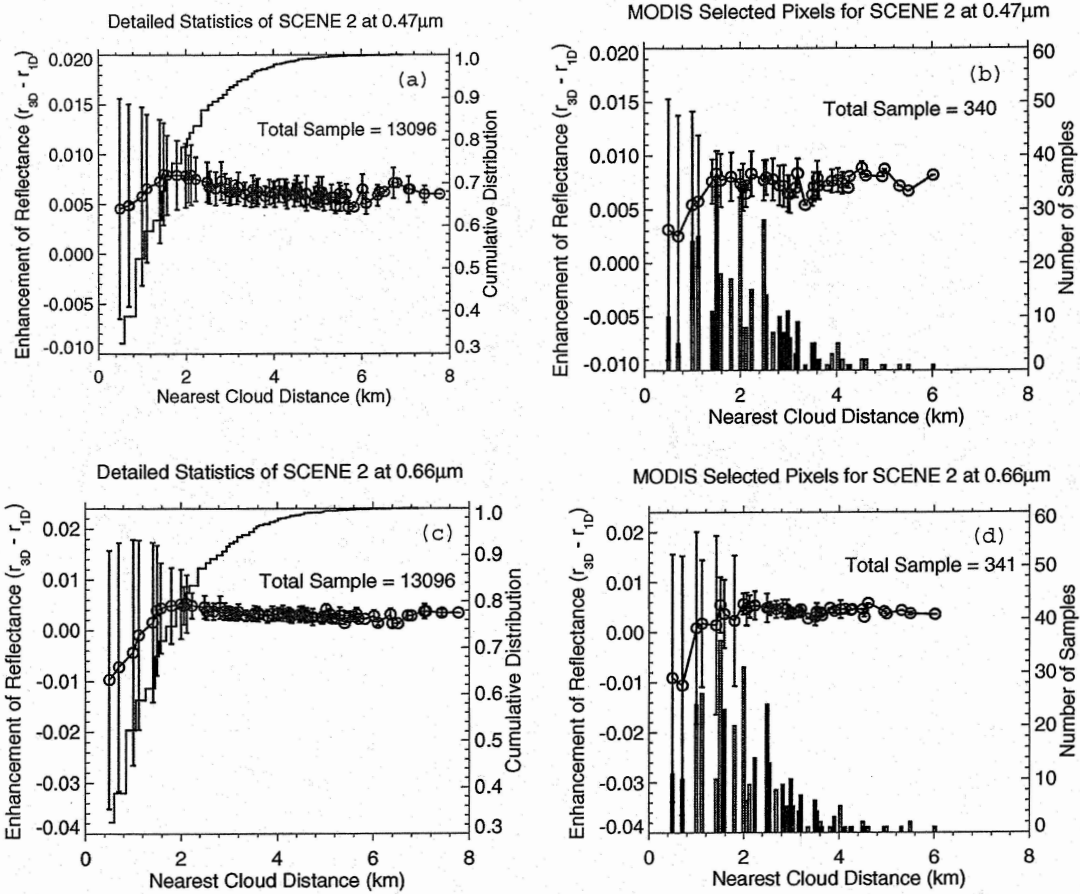


Figure 9. Average enhancement (circles, left scale) and standard deviation (vertical brackets) for clear pixels as a function of the nearest cloud distance. Cumulative and sample distributions of clear pixels as a function of the nearest cloud distance (right scale) for scene 1. Results are (a) and (c) for all non-cloudy pixels at wavelengths $0.47\mu\text{m}$ and $0.66\mu\text{m}$ respectively. Results for MODIS selected pixels are presented in (b) and (d) respectively.

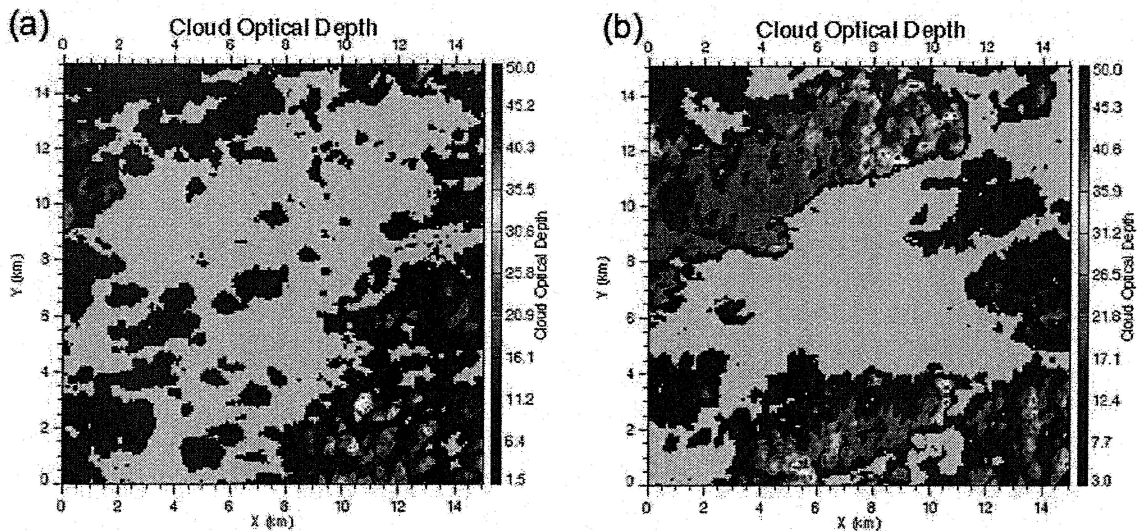


Figure 10. Cloud optical depth retrieved from an ASTER image collocated with Scene 1. Shown are two subsets of the image both at 90 m resolution designated in Fig 2a as the two boxes outlined in black (a) for upper box, and (b) for lower box of shown in Fig. 2a. The averages of cloud optical depth and standard deviations are τ (thin clouds) ~ 7 and σ (thin clouds) ~ 6 ; τ (thick clouds) ~ 14 and σ (thick clouds) ~ 8 . The cloud cover is $\sim 51\%$ and $\sim 59\%$ for (a) and (b) respectively.

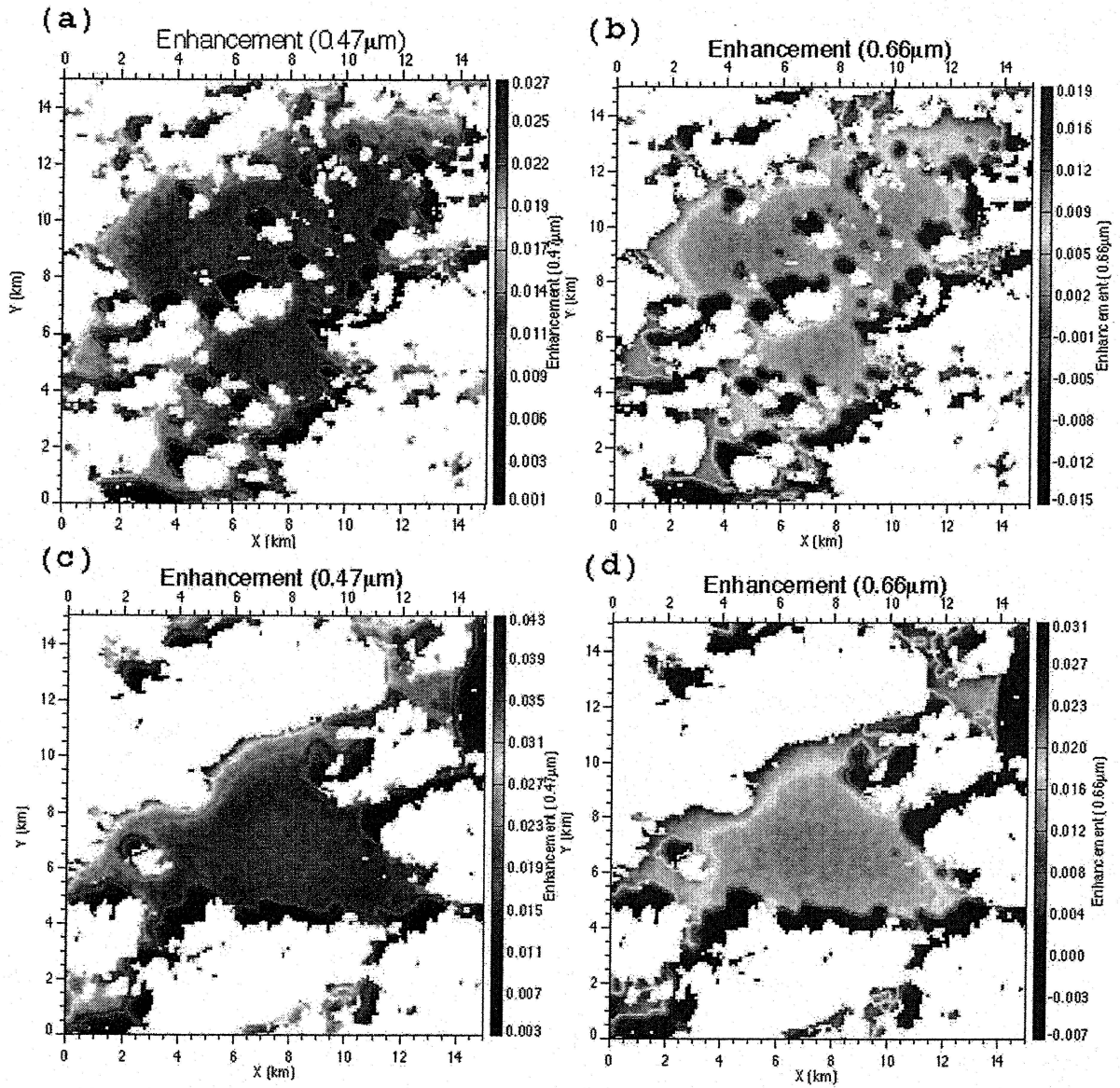


Figure 11. Enhancement of reflected solar radiation due to 3D effects for clear regions in thin (upper panel) and thick cumulus (lower panel) for wavelengths at $0.47 \mu\text{m}$ (left) and $0.66 \mu\text{m}$ (right) at 90 m resolution. Cloud pixels are masked as white. For the thin cloud field $\overline{\Delta r}_{0.47 \mu\text{m}} = 0.012$ and $\sigma_{0.47 \mu\text{m}} = 0.004$; and $\overline{\Delta r}_{0.66 \mu\text{m}} = 0.0018$ and $\sigma_{0.66 \mu\text{m}} = 0.007$. For the thick cloud field $\overline{\Delta r}_{0.47 \mu\text{m}} = 0.019$ and $\sigma_{0.47 \mu\text{m}} = 0.006$; and $\overline{\Delta r}_{0.66 \mu\text{m}} = 0.01$ and $\sigma_{0.66 \mu\text{m}} = 0.009$. The color bar stretch is different for each panel.

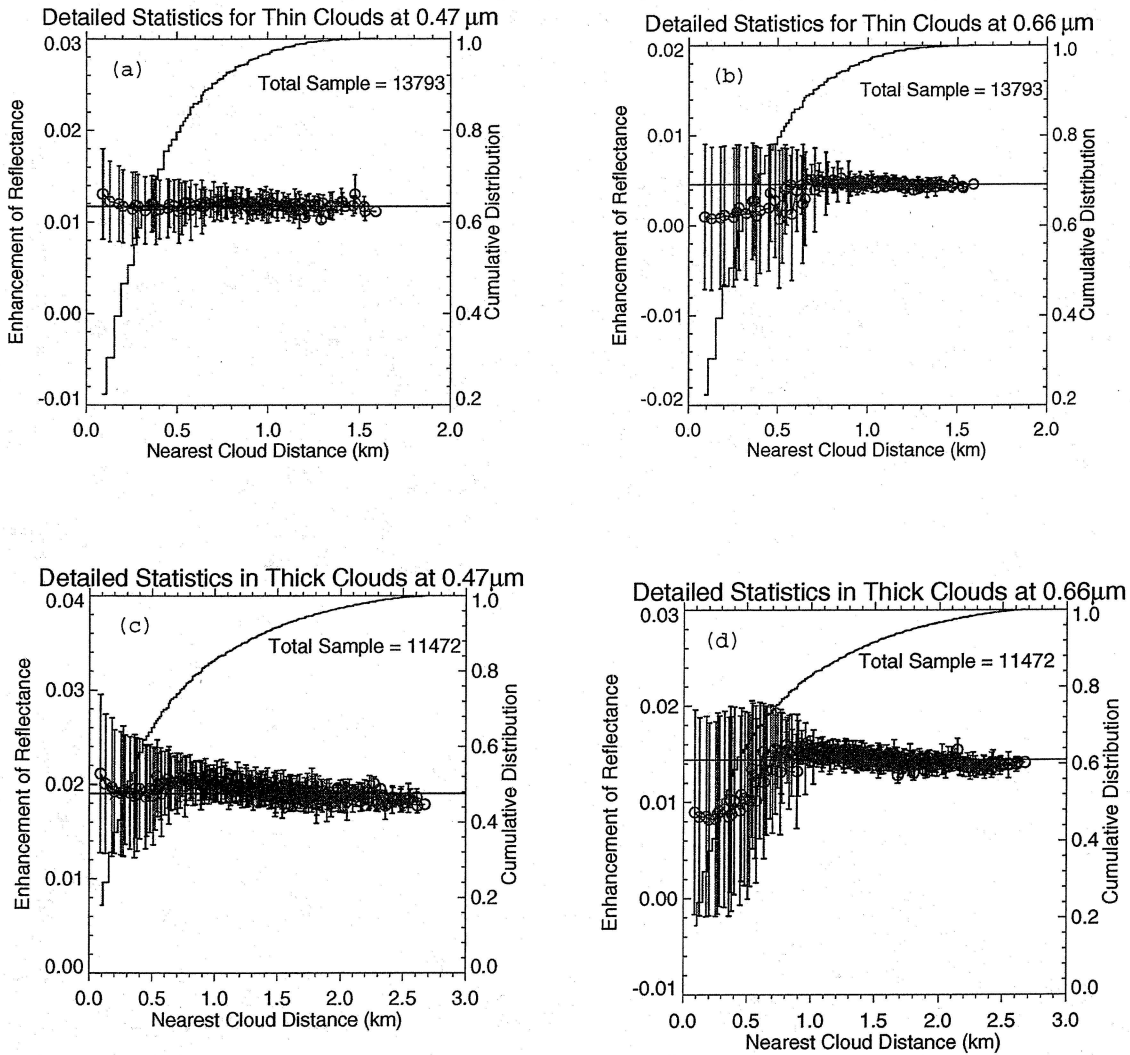


Figure 12. Similar to Fig. 7 but for detailed statistics of the enhancement of reflectance in the finer resolution images of Fig. 11. The upper panels show the enhanced reflectance as a function of cloud distance and cumulative distribution for the image with optically thin clouds. The lower panels show the same for the image with thicker clouds. The left panels are for $0.47 \mu\text{m}$ and the right for $0.66 \mu\text{m}$.